JACS
JOURNAL OF THE AMERICAN CHEMICAL SOCIETY

Article

pubs.acs.org/JACS

Revealing Chemical Processes Involved in Electrochemical (De)Lithiation of Al with *in Situ* Neutron Depth Profiling and X-ray Diffraction

Danny X. Liu and Anne C. Co*

Department of Chemistry and Biochemistry, The Ohio State University, Columbus, Ohio 43210 United States

Supporting Information

ABSTRACT: Herein we report a direct measurement of Li transport in real-time during charge and discharge process within an Al matrix using neutron depth profiling (NDP). *In situ* NDP was used to reveal and quantify parasitic losses during the first 25 mAhr/g of lithiation, followed by the formation of LiAl protrusions from the surface of pristine Al. Evidence of Li entrapment is also reported during delithiation. Subsequent lithiation and delithiation showed electrochemical charge passed to be equivalent to the amount of lithium incorporated into the Al matrix with negligible difference, suggesting that the parasitic losses including the formation of the solid electrolyte layer may be confined to the first lithiation. Parallel *in situ* XRD measurements also confirm the transformation of β-LiAl from a solid solution of α-LiAl, revealing solid solution-mediated crystallization of β-LiAl.

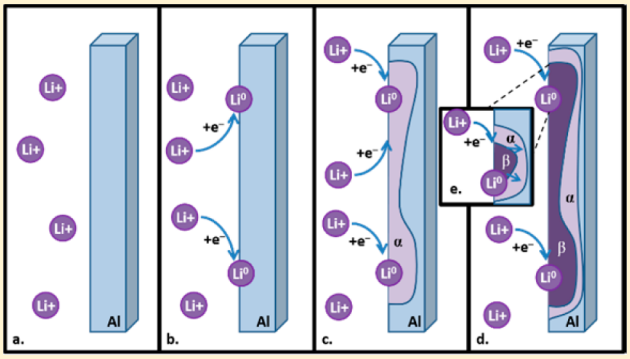

INTRODUCTION

Nondestructive methodologies for probing reaction dynamics, transient processes, and materials transformations in real-time are crucial for advancing our understanding of materials function, reaction processes, and failure mechanisms under operating conditions, such as those in an operating battery. *In situ* X-ray diffraction (XRD), nuclear magnetic resonance, transmission electron microscopy, synchrotron X-ray tomography,[1−6] and neutron depth profiling (NDP)[7−15] have been used to probe crystal structure evolution, visualize the expansion/contraction of electrode materials during lithiation and delithiation, quantify lithium distribution and transport, and provide mechanistic insights into the kinetics and nonequilibrium processes occurring in a battery. In this work, we report the real-time transport of Li from the measurement of spatial and temporal distribution of Li upon charge and discharge and the evolution of phases in LiAl alloys using *in situ* NDP and XRD, respectively.

LiAl alloys are commercially important materials for structural applications in aerospace due to their high strength-to-weight ratio,[16] high elastic modulus, and low density. They have been used as a blanket material for nuclear fusion reactors[17] and as additives to metallized propellants[18] and have been intensively studied as anodes for energy-storage devices.[19,20] Al provides theoretical storage capacity of 993 mAhr/g as an anode, almost 3 times that of conventional graphite (375 mAhr/g), while maintaining a large voltage window. Al is environmentally benign, abundant, and inexpensive, while generally exhibits poor cyclability and low Coulombic efficiency, which has limited its application as a secondary battery electrode.

It is generally thought that drastic structural changes during charge and discharge result in slow kinetics and poor cycle life. Significant research in materials capable of bypassing crystallographic transitions, and instead incorporate lithium through electrochemically driven amorphization processes, such as Li into Si, SnO_2, ZnO_2, and Ge,[21−24] has been reported. Li-ion battery material that forms solid solution with Li over a large compositional range with no phase transformation has also been shown to have high-rate capabilities.[25−32] Examples include $Li_{1.06}Mn_2O_{4.1}$ that forms a solid solution throughout the delithiation process,[33] as does $LiFePO_4$,[25−28] which some argue to be a moving phase boundary instead of solid solution.

Al forms solid solutions with Li, referred to as α-LiAl, where the lattice strain energy can be reduced with the incorporation of the larger Li atoms. During the charge/discharge process, Li is electrochemically driven into the matrix where the solid solution acts as a reaction front transporting lithium to energetically favorable sites. The formation of a α-LiAl precedes and facilitates the crystallization of β-LiAl intermetallic. Electrochemical amorphization was not observed in LiAl,[21] suggesting that electrochemical lithiation through a solid solution-mediated pathway to crystallization to be fundamentally different from the amorphization pathway. In addition to structural effects, Coulombic efficiency and cycle life are also greatly influenced by other parasitic reactions occurring in an

Received: October 1, 2015
Published: December 4, 2015

DOI: 10.1021/jacs.5b10295
J. Am. Chem. Soc. 2016, 138, 231−238

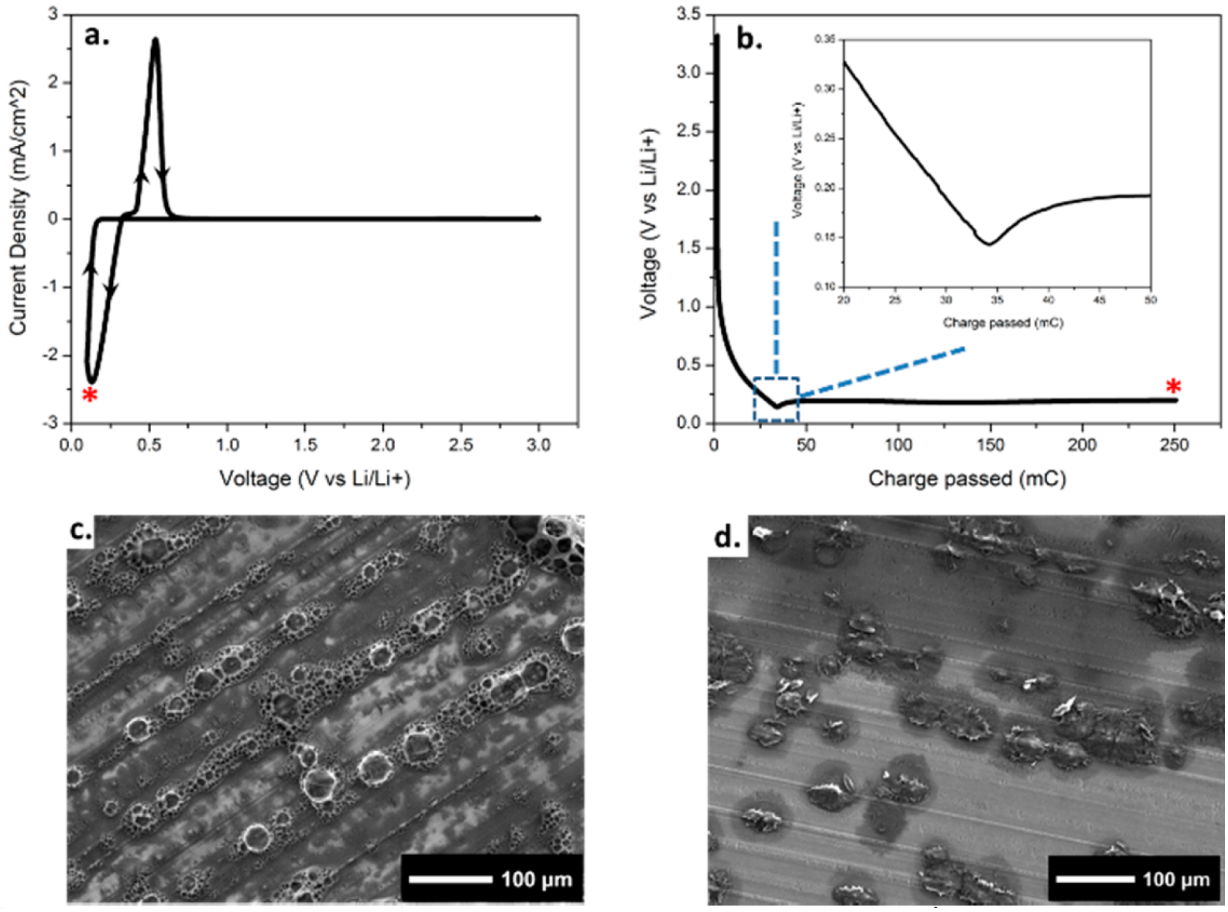

Figure 1. (A) Cyclic voltammogram of Al foil in 1 M $LiPF_6$ EC:DMC (1:1 vol) (Novolyte) at 50 μV/s. (B) Galvanostatic lithiation of Al foil at 24.4 $\mu A/cm^2$ 1 M $LiPF_6$ EC:DMC (1:1 wt) (Selectilyte). SEM (C) at the reduction peak at 0.13 V vs Li/Li^+ denoted by asterisk in (A) and (D) at the voltage plateau in (B) after 250 mC of charge passed, denoted by asterisk. The samples were assembled in an Ar-filled glovebox (O_2 and H_2O < 0.5 ppm). Measurements were made in a three-electrode Swagelok-type cell using a Li metal ring reference electrode and a Li disc counter electrode. All lithiated samples were washed with 3 mL of acetone prior to SEM characterization.

operating battery, such as electrochemical reactions with the electrolyte and electroreduction of surface oxides. Trapping of Li within localized pockets in the electrode also leads to low Coulombic efficiency. Nonetheless, fundamental understanding of dynamic processes occurring during charge/discharge, leading to phase evolution at nonequilibrium conditions, rearrangement of Li atoms such as those observed in Li_xSn[9] with and without an applied load, formation and distribution of electrolyte byproducts at interfaces is still deficient and would benefit from real-time characterization under dynamic operating conditions.

Reported herein is the real-time quantification of Li distribution and transport during charge/discharge using neutron-induced nuclear reactions. NDP has a high sensitivity toward light elements such as ^{6}Li, ^{10}B, ^{14}N, and ^{7}Be. The selective nature of neutrons results in spectra that allows for direct tracking and counting of Li atoms. This paper presents *in situ* NDP for the direct measurement of Li transport and reveals self-discharging phenomenon for electrodes at rest, the formation of Li-enriched surface protrusions, and the entrapment of Li within the matrix. In addition, real-time XRD measurements were employed to confirm the transformation of β-LiAl from a solid solution of α-LiAl, revealing solid solution-mediated crystallization.

EXPERIMENTAL SECTION

Three-Electrode Electrochemical Measurements. Electrochemical measurements were performed in an in-house designed, sealed, three-electrode half-cell. A 12 mm diameter Al disc (0.016 mm thick, 98.5+%, Reynolds Co.) was used as the working electrode, with a 12 mm metallic Li disc (Chemetall Foote Corp.) as the counter electrode and a 12 mm diameter Li ring as a reference electrode. The electrolyte was a 1 M $LiPF_6$ in 1:1 vol EC:DMC (Novolyte) or 1 M $LiPF_6$ in 1:1 wt EC:DMC (Selectilyte).

Two-Electrode Coin Cell Assembly for XRD and NDP Measurements. A 12 mm diameter Al disc (0.016 mm thick, 98.5+%, Reynolds Co.) and a 12 mm diameter metallic lithium (Chemetall Foote Corp.) separated by a 25 μm-thick separator (Celgard) in a 1 M $LiPF_6$ in 1:1 vol EC:DMC (Novolyte), 1:1 wt EC:DMC (Selectilyte), or 1 M LiBF4 in 1:1 wt EC:DMC (Sigma) was assembled in a modified CR2032 coin cells (MTI Corp). Coin cell components were cleaned in acetone (≥99.5%) and methanol (≥99.8%) sequentially, followed by overnight drying at 55 °C under vacuum. The coin cells were crimped using a manual hydraulic crimping machine (MSK-110, MTI Corp) equipped with a CR2032 die at pressures of 1100−1200 psi. The coin cells were modified with a 9.5 mm diameter hole on one of the casings to allow the placement of a Kapton film (7.5 μm thickness) adhered to the casing via Kapton tape. The electrochemical cell remains functional and air free for weeks and remains "leak" free under vacuum (10^{-3}−10^{-7} Torr) for days.

The handling of materials and the assembling of the three-electrode cells and the Kapton modified coin cells were performed in an Ar-filled glovebox (mBraun) with continuous H_2O (<0.5 ppm) and O_2 (<0.5

DOI: 10.1021/jacs.5b10295
J. Am. Chem. Soc. 2016, 138, 231−238

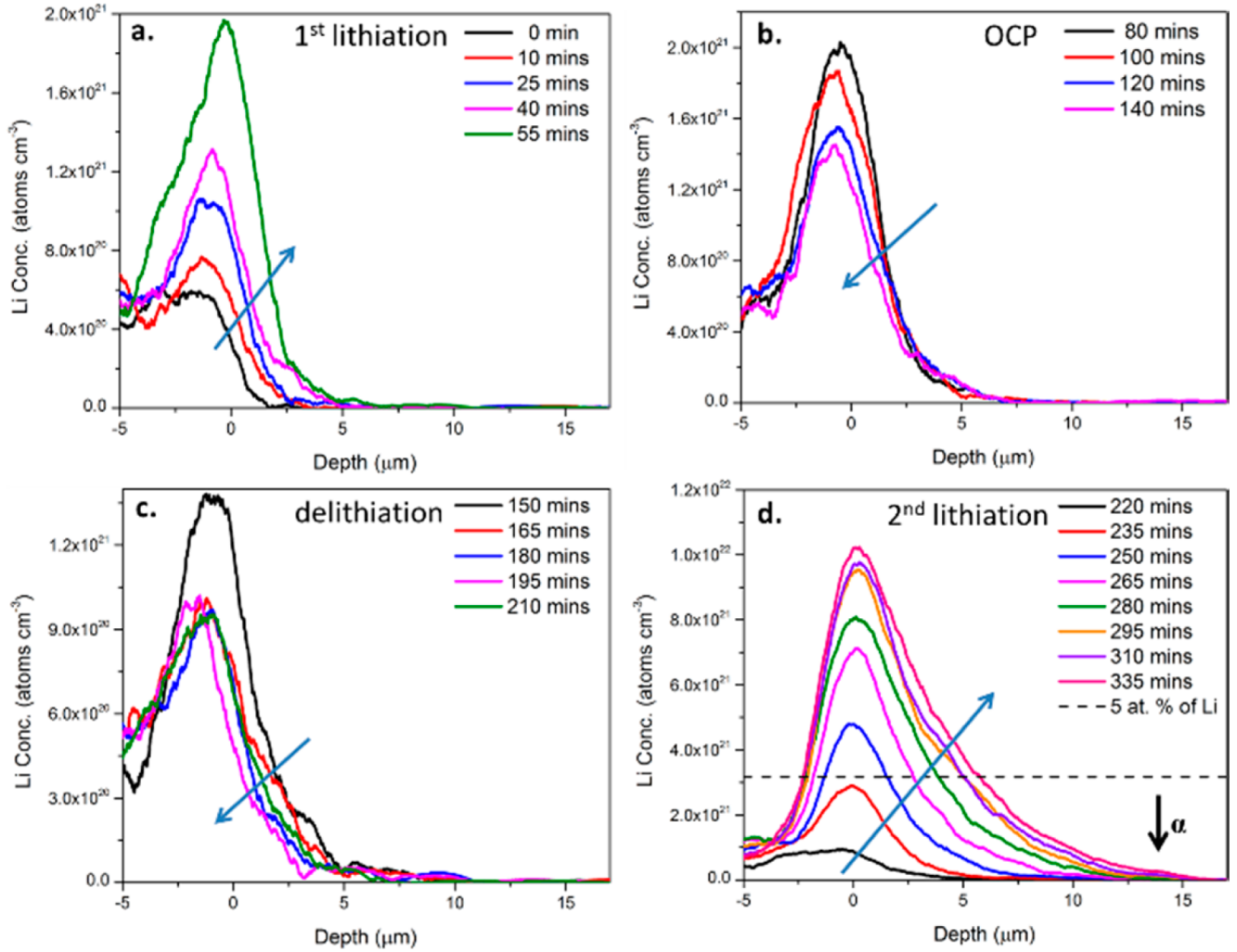

Figure 2. Li concentration profiles across the electrode/electrolyte interface and within a 16 μm Al foil as a function of time. (A) Lithiation spectra between 0 and 60 min at 0.2 V vs Li/Li^+; (B) lithium distribution at open circuit between 65 and 145 min; (C) delithiation at 0.5 V vs Li/Li^+ between 150 and 215 min; and (D) second lithiation at 0.2 V vs Li/Li^+ between 220 and 335 min. The sample was assembled in an Ar-filled glovebox (O_2 and H_2O < 0.5 ppm) using a Kapton window modified 2032 coin cell, with a Li metal serving as both the counter and reference electrodes and a Celgard 2400 separator in 1 M $LiBF_4$ in EC:DMC (1:1 wt). The working electrode area is 1.2 cm^2. A 5.5 mm diameter circular Teflon aperture was used for NDP measurements.

ppm) detection. After assembly, the sealed three-electrode cells were transported to the bench or another Ar-filled glovebox (LC Technology) for testing. The Kapton modified coin cells were transported to NIST in a sealed Ar-filled desiccator. Electrochemical measurements were performed on a Gamry potentiostat (Reference 600, Gamry Instruments). The mass of the electroactive Al electrode was determined by weight. All voltages measured were reported against Li/Li^+.

XRD Instrumentation. XRD patterns were collected using a Bruker Advance D8 equipped with a position sensitive detector. Data were collected using DIFFRAC plus XRD Commander software version 2.6.1 from 20° to 70° 2θ with step size of ~0.015° at a rate of 1 s/step using a Ge (111) monochromated Cu Kα_1 radiation (λ = 1.54056 Å; 40 kV, 50 mA). The angular accuracy was calculated to be ±0.07° by measuring the fwhm of the 35.15 2θ peak in corundum (NIST SRM 1976 standard). *In situ* measurement was obtained using the same modified Kapton window coin cell used in the *in situ* NDP experiment.

NDP Instrumentation and Calibration. Data presented in this paper were obtained using a "cold" NDP facility at the National Institute of Standards and Technology's (NIST) Center for Neutron Research (NCNR) (Gaithersburg, MD, USA), while the optimization of the electrochemical design and preliminary *in situ* testing were initially performed at The Ohio State University Research Reactor. The facility at NIST provides[34] a well-collimated "cold" neutron (~5 meV) with thermal equivalent fluence rate of 1 × $10^9/cm^2$ s and a nominal beam area of 110 mm^2. Additionally, a neutron monitor is operated concurrently with all determinations to correct for any minor variations in fluence rate when necessary, historically around 1% over a reactor cycle. The measured sample area was defined by a 5.5 mm diameter circular aperture in a Teflon mask.

NDP is a quantitative analytical technique for measuring certain elements that absorb neutrons as a function of depth. ^6Li absorbs neutrons (with a cross-section of 938 barns for neutron energy at 25 meV and 2355 barns at 4 meV) governed through the following nuclear reaction:

$$^6Li + n \rightarrow {}^3H(2727.9\ keV) + {}^4He(2055.5\ keV) \quad (1)$$

The energy spectrum of the triton particles is quantified, and their corresponding depth from which the particles originated from can be directly determined based on the atomic composition and density of the electrode material. Details regarding the energy, depth, and concentration calibration can be found in our previous reports and in the Supporting Information.[9,11]

DOI: 10.1021/jacs.5b10295
J. Am. Chem. Soc. 2016, 138, 231−238

RESULTS AND DISCUSSION

A voltammogram of Al in 1 M $LiPF_6$ in EC:DMC (1:1 vol %) is displayed in Figure 1a showing a hysteretic reduction peak at 0.13 V and a corresponding oxidative peak at 0.54 V. The first cycle typically comprises a single, hysteretic reduction peak at 0.13 V and a corresponding oxidative peak at 0.54 V. A charge of 3.57 C was passed during the reductive lithiation of Al, determined from the integrated area under the curve between the forward and reverse sweep of the reductive peak. A 2.66 C of charge was measured from the integrated area under the oxidative current corresponding to the delithiation of Al. The 74.5% round-trip Coulombic efficiency of Al lithiation/delithiation is typical of those reported in the literature.[35]

SEM images in Figure 1c,d correspond to the surface morphology at the reduction peak at 0.13 V (Figure 1a) and after the potential plateau in Figure 1b, respectively. The potential plateau arises when the voltage becomes invariant as a function of composition. The potential plateau indicates a two-phase equilibrium between α- and β-phases of LiAl, as described by the Gibbs phase rule (see Supporting Information for derivation). The SEM images clearly show raised physical features on the order of 25−50 μm surrounded by a darker contrast, preferentially along the machining lines. Regions of dark contrast suggest different species or stages of Al lithiation. It is important to note that the protruded features and the varying shades from the scattered electrons are not observed on pristine Al surfaces (Supporting Information). These raised features could be attributed to the nucleation of a Li_xAl phase[8,36] which reaches a terminal length of 50 μm. β-LiAl has been proposed to nucleate and grow spherically, in three dimensions, within the α-LiAl solid solution.[37] The spherical nuclei protruding outward are due to an increase in the unit cell of an α-LiAl solid solution, ranging between 4.042 and 4.050 Å, contracting as the Li concentration increases to 10 at%, to a β-LiAl phase unit cell of 6.356−6.370 Å[38] (46−57 at% Li). The electrochemical and SEM results confirm nucleation-growth as the dominant process during the initial stages of Al lithiation.

The formation of β-LiAl involves the electrochemical incorporation of lithium into a solid solution of α-LiAl reaching supersaturation, followed by the crystallization of the β-LiAl[36,37,39] intermetallic. In an electrochemical cell where lithiation is sustained at a constant rate, lithiation originating at the Al electrode/electrolyte interface will eventually propagate into the bulk material where the transport of Li generally limits the rate of lithiation and therefore formation of the α- and β-LiAl. We have previously reported an *in situ* neutron-based technique for probing Li transport during the formation and removal of a Li_xSn intermetallic through a charge and discharge cycle.[9] NDP is a nondestructive technique for quantifying the amount and the location of lithium within the electrode material.[7,9,40] Performing NDP *in situ* allows the quantification of Li transport during active charge/discharge as well as Li relaxation dynamics immediately after the removal of the current or potential perturbation. Herein, *in situ* NDP is employed to quantify Li content and probe its position with time, obtaining Li transport measurements in Al during lithiation and delithiation.

A series of lithium concentration profiles in Al is displayed in Figure 2. The "0 μm" on the depth scale was determined using the interface between the unlithiated Al in contact with 1 M $LiBF_4$ in 1:1 wt % EC:DMC (Figure 2a, 0 min). Thus, the Al electrode/electrolyte interface is defined as "0 μm". Positive depth values of up to 16 μm encompass the thickness of the Al electrode. Negative depth values represent the electrolyte region. Prior to lithiation, the only lithium signal detected in the electrolyte region (−5 to 0 μm) corresponds to 1 M Li^+ in the electrolyte (Figure 2a, 0 min).

During the lithiation process, the amount of lithium is observed to increase significantly first at the electrode/electrolyte interface before propagating approximately 2 μm into the Al electrode. Interestingly, an equally significant amount of Li signal increase is also found to extend into the electrolyte region between 0 and −5 μm, with a shoulder developing at −2.5 to −3 μm at 55 min (ca. 4 mAhr/g Al) into the lithiation process. This 2.5 μm protrusion is indicative of the initial nucleation of β-LiAl, observed in the scanning electron micrograph (SEM) images in Figure 1. This shoulder is less pronounced during subsequent OCP resting period, delithiation, and second lithiation (Figure 2b−d, respectively), while the amount of absolute integrated Li charge in the "electrolyte" region is not negligible. Other possible contributions to the increased Li concentration in the electrolyte region include Li counts from (i) Li-containing solid electrolyte interface (SEI) formed and (ii) Li−Al−O glass layer[41] which can be formed during the electrochemical reduction of the native Al_2O_3 in the presence of Li. In this work a 4 nm native oxide on Al is confirmed via XPS (Supporting Information).

Following the first lithiation, a resting period in which no potential was applied was monitored as shown in Figure 2b (i.e., Li NDP was collected at OCP). Unlike the phenomena observed in Sn lithiation, where Li atoms continued to diffuse and rearrange within the material when the applied potential is removed,[9] lithiated Al is shown to "self-discharge" upon which a decrease in lithium concentration, equivalent to around 1 mAhr/g Al is measured over 60 min (80 to 140 min in Figure 2b). Subsequent delithiation at 0.5 V following the OCP period (Figure 2c) showed significant decrease in the Li concentration (2 mAhr/g Al) between −4.5 to 5 μm region within 150 to 165 min. Notably, a substantial amount of Li was also removed in the electrolyte region, possibly due to the oxidation and partial removal of the SEI and/or Li−Al−O glass layer. Nevertheless, even at the end of the delithiation period, the concentration of the Li atoms in the electrolytes remains higher than the original 1 M electrolyte concentration of 4×10^{20} Li atoms/cm^3, indicating that the lithium-containing surface layer is not completely removed. In addition, delithiation at 0.5 V revealed that the Li concentration attenuates toward steady state, indicating that some Li can remain trapped within the Al matrix. From the concentration data in Figure 2c, we surmise that the Li within the Al matrix to be less than the 5% solubility limit for the β-phase to nucleate,[39] therefore the composition at this stage should predominantly be α-LiAl which has been reported to have a lower Li diffusion rate than β-LiAl (Supporting Information).[36] This Li entrapment would result in lower Coulombic efficiency observed.[36,39]

The Li concentration profile of a second lithiation at 0.2 V, shown in Figure 2d, resembles those of Sn lithiation[9] after the initial formation charge/discharge cycle. A significant increase in Li concentration is observed over 115 min period (between 220 and 335 min, corresponding to a capacity of 46 mAhr/g Al). Initially, Li is shown to increase rapidly at the surface approaching 1.1×10^{22} atoms/cm^3. Eventually, Li propagates throughout the entire 16 μm-thick Al foil with Li profiles exhibiting the highest concentration near the surface and monotonically decreasing into the bulk. Higher rates and

DOI: 10.1021/jacs.5b10295
J. Am. Chem. Soc. 2016, 138, 231−238

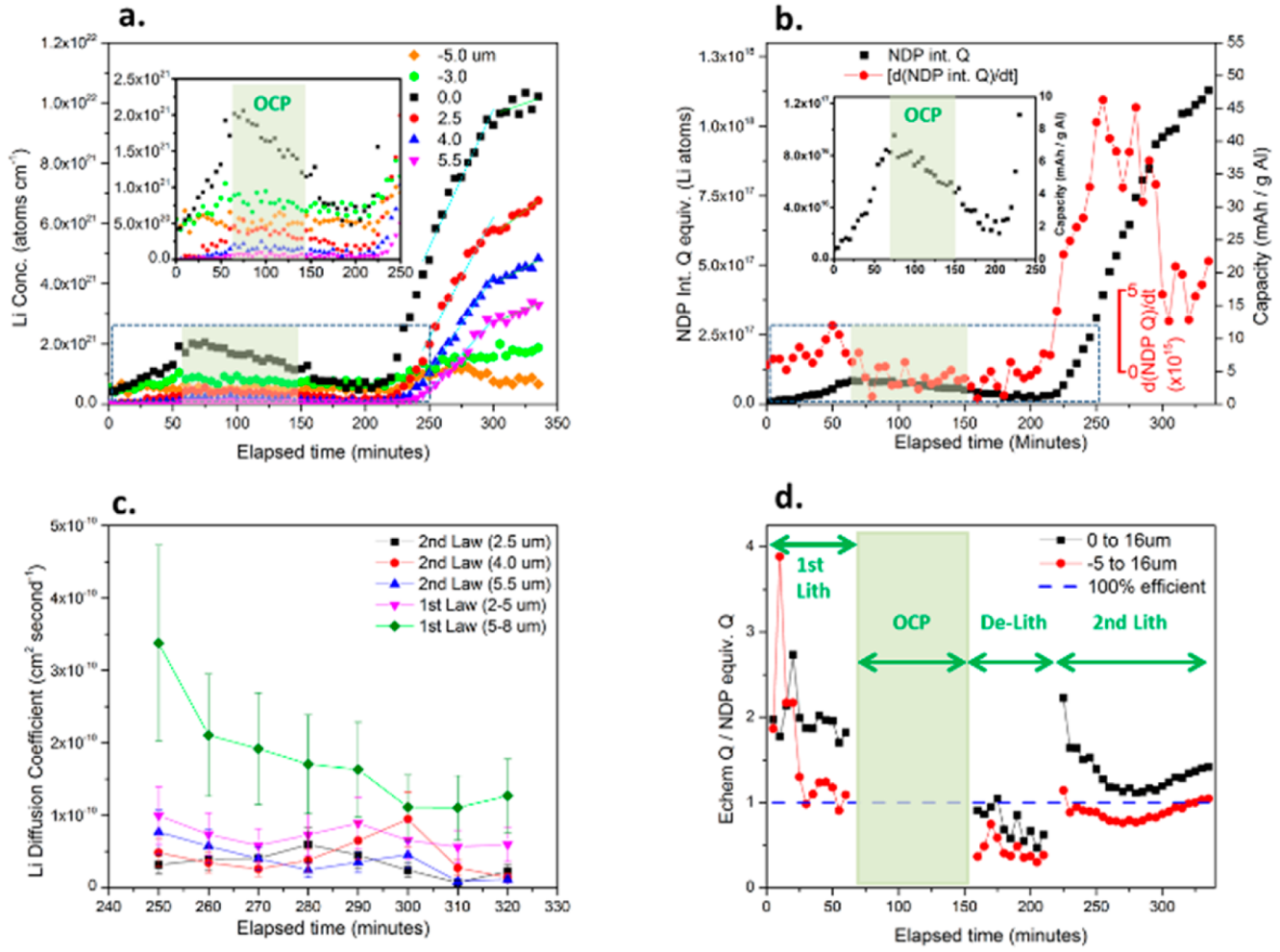

Figure 3. (A) Li concentration at various depths as a function of elapsed time. First lithiation at 0.2 V between 0 and 60 min, followed by removal of the applied potential between 65 and 145 min, then delithiation at 0.5 V between 150 and 215 min, and second delithiation between 220 and 335 min. The inset highlights the first 250 min. (B) Total integrated Li and the change in Li concentration as a function of elapsed time. (C) Li diffusion coefficient in Al obtained from Fick's first and second law during the second lithiation. The error bars represent an estimated 40% uncertainty resulting from the variation within the electrode composition, calculated based on the percent difference between the depths that at triton charge particle could traverse through in Al vs LiAl. (D) Ratio of electrochemical charge passed to the charge equivalent to the integrated Li as a function of the elapsed time.

amounts of lithiation are measured during the second lithiation at 0.2 V, while the amount of Li accumulating on the electrolyte side remained constant after 250 min (10 mAhr/g) of lithiation, suggesting that the formation cycle is predominantly during the first lithiation.

The rate of lithiation is represented in Figure 3a, where the Li concentrations at various depths were plotted as a function of time. It is evident that the highest rate of lithiation and delithiation, as measured by the magnitude of the slope of Li concentration vs time, is greatest at the surface (0.0 μm). Lithiation rates decrease significantly further away from the electrode/electrolyte interface. There is also a notable decrease in the rate of Li incorporation into the material after 295 min, observed at all depths.

Quantitative measurement of lithium atoms can be obtained through the integration of the area under each concentration profile shown in Figure 2. Details in the method of quantification are described in our previous paper.[9] The total integrated lithium atoms within the electrode material (0 to 16 μm) are plotted as a function of time in Figure 3b (square trace), whereas the circle trace is the corresponding first derivative (dQ_{NDP}/dt), indicating rates of lithiation over the entire electrode and the interface. A steady electrode lithiation rate is observed during the first lithiation. When the applied potential is removed, a "self-discharge" rate is 6×10^{12} atoms/s or equivalent to 4 μA/cm^2, assuming that all the Li during the self-discharge goes through a one electron process to form a Li^+ or Li-containing species. The "self-discharge" current measured is in good agreement with the observations reported by Maskell et al.[36] of 1 to 2.5 μA/cm^2. During delithiation, the slope of the Li NDP charge was similar to that during the OCP period. This suggests that the majority of the delithiation current was used to oxidize species on the surface (outside of the integration limits of 0−16 μm). The second lithiation of Al again shows similarities to those of Sn lithiation, where lithium incorporation does not occur in uniform increments, where the lithiation rates generally decrease as the surface is saturated with Li atoms.

The diffusion coefficients at various depths corresponding to the second lithiation were compared using the calculated value obtained from the Fick first and second laws. Only the second lithiation diffusion coefficient was calculated since the first

DOI: 10.1021/jacs.5b10295
J. Am. Chem. Soc. 2016, 138, 231−238

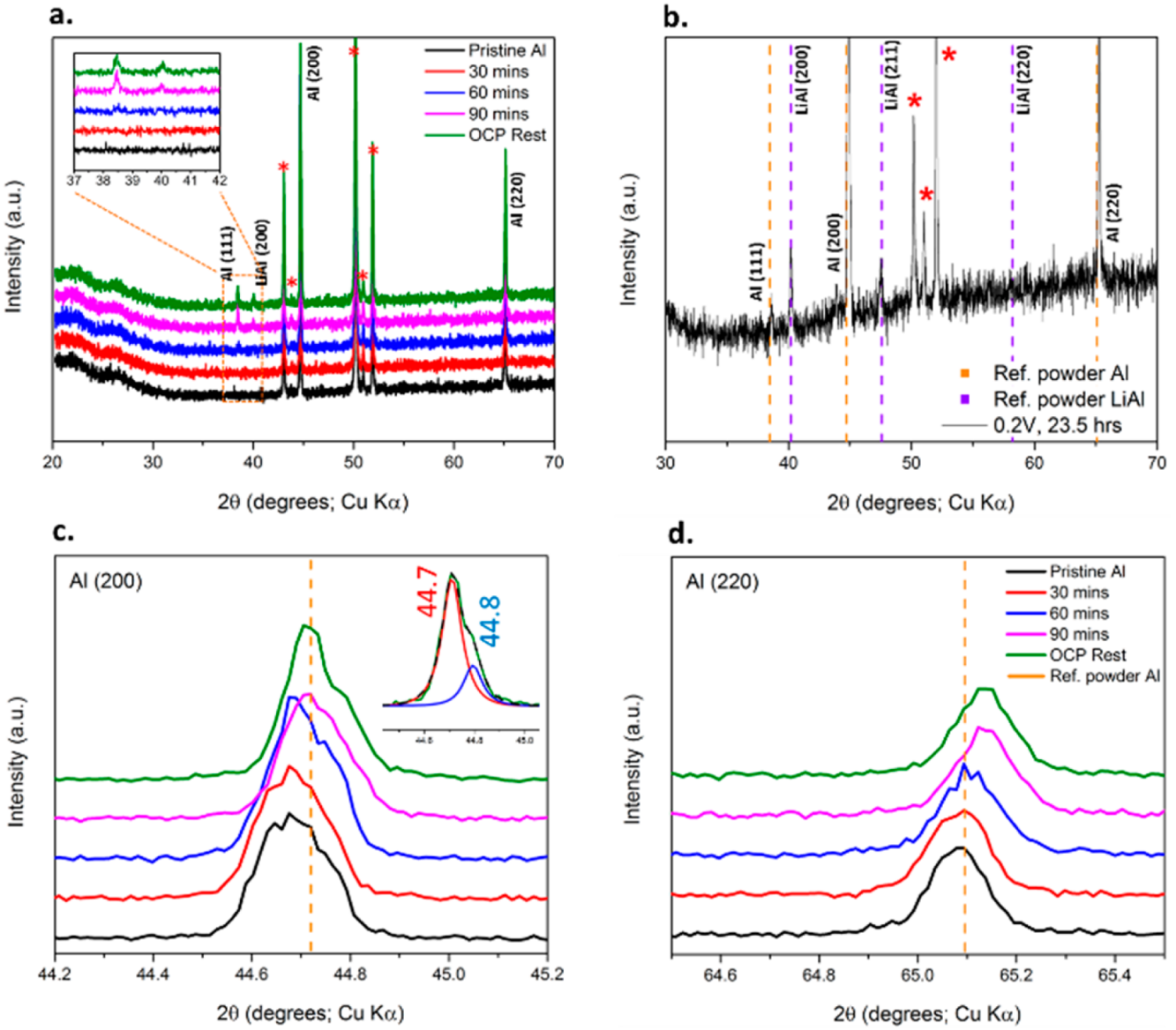

Figure 4. (A) *In situ* XRD patterns of Al electrode collected at 30 min intervals while being lithiated at 0.2 V vs Li/Li^+. Inset reflects *in situ* XRD patterns within the 37−42 2θ region. (B) *Ex situ* XRD of Al foil lithiated at 0.2 V for 23.5 h. (C) Al (200) and (D) Al (220) reflections showing a shift to higher 2θ values as a function of lithiation time. Inset in (C) shows 2 Gausian function fitted to the XRD collected at OCP after 90 min of lithiation. XRD was measured with a Cu Kα source. All raw patterns were shifted by +0.3° 2θ to account for sample height displacement. The * indicate contributions from the experimental setup. The sample was assembled in an Ar-filled glovebox (O_2 and H_2O < 0.5 ppm) using a Kapton window modified 2032 coin cell, with a Li metal serving as both the counter and reference electrode, and a Celgard 2400 separator in 1 M $LiBF_4$ in EC:DMC (1:1 wt). The working electrode area is 1.2 cm^2.

lithiation may contain considerable parasitic contributions as exemplified in Figure 3d. Figure 3d shows the ratio between the electrochemical charged passed and the charge equivalent to the amount of Li detected by NDP. Ideally, the ratio of the charge passed should be 1. A ratio larger than 1, as observed in the square trace of the first lithiation (between 0 and 16 μm), indicates parasitic reactions on the electrode that are consuming electrons. Once all of the Li from within the Al, interface, and electrolyte (integrate region between −5 to 15 μm) are accounted for (circle trace), the ratio between electrochemical Q/NDP Q approaches 1 at >25 min, indicating that the "parasitic loses" between 25 and 60 min, are essentially due to the formation of the LiAl protrusions or Li-containing SEI. Between 0 and 25 min, the parasitic losses or electrons are consumed in processes not involving Li (thus not detected via NDP), which could include the reduction of the Al surface oxide or reduction of the solvent.

During the second lithiation (220 to 335 min), the ratio of the electrochemical Q/NDP Q approaches 1. The contributions from the electrolyte are assumed to be minimal such that the electrochemical current can be used to approximate the lithium flux. Diffusion coefficient of Li in Al has been reported to range between 10^{-6} and 10^{-16} cm^2/s. A literature survey of available Li diffusion coefficient for α-LiAl and β-LiAl is tabulated in the Supporting Information. In this work, the effective Li diffusion coefficient obtained from the direct observation of Li transport within Al is averaged to be 4.7(±2) × 10^{-10} cm^2/s. While the diffusion coefficient was calculated separately as a function of depth, the resulting values are not statistically different, and therefore the effective diffusion

DOI: 10.1021/jacs.5b10295
J. Am. Chem. Soc. 2016, 138, 231−238

coefficient reported herein neglects the effects of depth. Also, the data used to calculate this value were limited to a region where the dominant LiAl species is the β-phase. Experimentally, the effective diffusion coefficient was only obtained from data available above the horizontal dash line in Figure 2d, which is the α-phase solubility limit of 5% Li.[39]

In situ XRD was used to confirm the mechanism of Al lithiation which goes through an initial α solid solution phase followed by the nucleation of a β-LiAl phase.[39] Figure 4a shows *in situ* XRD measurement of a pristine Al and its subsequent lithiation until a LiAl intermetallic phase is observable. First of all, initial pristine Al presents a systematic absence of the Al (111) reflection, suggesting preferential orientation in the Al foil. This is common in metal foils as a result of a tendency for a grain to undergo slip and rotation during the manufacturing process.[42] A small (<1%) but barely detectable Al (111) peak is observed when Al foils were annealed to 630 °C for 4 h with a heating rate of 5 K/min and cooling rate of 1 K/min to relieve the stress within Al and to provide sufficient energy to reorient the Al domains. This indicates that the Al foil indeed has a preferred orientation and thus the absence of the Al (111).

The Al foil was lithiated at 0.2 V, while XRD patterns were collected in 30 min intervals. While initially absent, the Al (111) reflection appeared after 60 min of lithiation (after 0.55 mAhr of charge passed), suggesting a rearrangement in the Al domains due to the incorporation of Li, which is closely followed by the onset of a β-LiAl (200) at 1 mAhr after 90 min. A substantial contraction in the lattice is also observed from the shift in the Al (200) and (220) to higher 2θ values, shown in Figure 4c,d, between 60 and 90 min of lithiation. During the formation of a solid solution, a solute atom, such as Li, introduced into the host lattice, Al, can induce changes in the macroscopic lattice constants.[43] For example, it is known that as the Li concentration in the Al matrix increases to 5 at%, the lattice of the Al host contracts by 0.2% from 4.050 to 4.042 Å, whereas a nonstoichiometric β-LiAl expands by 0.22% from 6.356 to 6.370 Å[38,44] with increasing Li concentration from 46 to 57 at%.[38,44] A shoulder in the Al (200) is evident 90 min into the lithiation and remains when the voltage is removed. Figure 4c shows the fitted data corresponding to lattice constants of 4.050 and 4.042 Å, for the unlithiated Al and α-LiAl, respectively. The difference in the lattice parameter is consistent for a 0.2% contraction of the Al matrix when lithiated. Due to the low signal-to-noise resolution of *in situ* measurements, a separate sample was lithiated at 0.2 V vs Li/Li^+ for 23.5 h and then characterized (Figure 4b). Along with the β-LiAl (200) reflections, a new peak attributed to β-LiAl (211) was resolved, confirming the presence of the β-LiAl intermetallic.

There has been recent interest in investigating materials that form solid solutions. Solid solution appears to be a buffer region that mediates the nucleation of a stable phase, which helps explain the high rate capabilities of $LiFePO_4$.[25−28,45] Although recent modeling and experimental work suggested that the first-order phase transition of $LiFePO_4$ can be bypassed at high rates.[29−32] In contrast to other systems involving the electrochemical incorporation of lithium into the matrix including Si, Ge, ZnO, and SnO_2, the apparent lack of a solid solution phase may explain the electrochemically induced solid-state amorphization phenomenon,[21] in which large nucleation barriers and sluggish mass transport kinetics under ambient conditions prevent the formation of crystalline intermetallic species, resulting in a disordered amorphous material.[46] Crystallization generally involves nucleation of stable atomic or molecular clusters facilitating the subsequent growth of the nuclei, whereas some materials exhibit metastable states in existence instead of a direct transformation to the thermodynamically favorable crystalline state, as is the latter case in electrode amorphization, where the material may require a high activation to form the thermodynamically favorable crystalline intermetallic. On the other hand, it is plausible that a solid solution may provide a lower activated pathway to crystallization, through continuous lithiation of the matrix such that the system transforms from one transient state to another transient state with the smallest loss of free energy before reaching the most stable state, as described by Ostwald's rule of stages.[47] In this work, Al is lithiated at a very slow rate of 30 μA which is assumed to be sufficient to establish dynamic equilibrium.[48] The voltage plateau of 0.2 V describes an equilibrium between the α- and β-LiAl across a significant compositional range between 50 and 250 mC, which allows for a continuous change in composition favoring crystallization over amorphization.

■ ASSOCIATED CONTENT

Supporting Information

The Supporting Information is available free of charge on the ACS Publications website at DOI: 10.1021/jacs.5b10295.

NDP facility and calibration, lithium diffusion coefficient calculation, SEM images, XPS and XRD data, thermodynamic phases of LiAl (PDF)

In situ lithiation of Al (AVI)

■ AUTHOR INFORMATION

Corresponding Author

*co@chemistry.ohio-state.edu

Notes

The authors declare no competing financial interest.

■ ACKNOWLEDGMENTS

The authors thank Dr. R. Gregory Downing from NIST for useful discussions on NDP and the support from staff at The Ohio State University Nuclear Reactor Laboratory, Dr. Jinghui Wang and Prof Lei Cao for discussions on NDP calibration, Kwan Leung for collecting the SEM images, Nicholas Bashian for annealing the Al foil, and Sherwin Singer for discussion on Gibbs phase rule. This work was supported by the Department of Chemistry and Biochemistry at The Ohio State University and the National Institute of Standards and Technology (NIST) for the NIST Center for Neutron Research's (NCNR's) travel support to the Summer School on Methods and Applications of Small Angle Neutron Scattering and Neutron Reflectometry.

■ REFERENCES

(1) Blanc, F.; Leskes, M.; Grey, C. P. *Acc. Chem. Res.* **2013**, *46*, 1952.

(2) Huang, J. Y.; Zhong, L.; Wang, C. M.; Sullivan, J. P.; Xu, W.; Zhang, L. Q.; Mao, S. X.; Hudak, N. S.; Liu, X. H.; Subramanian, A.; Fan, H.; Qi, L.; Kushima, A.; Li, J. *Science* **2010**, *330*, 1515.

(3) Ebner, M.; Marone, F.; Stampanoni, M.; Wood, V. *Science* **2013**, *342*, 716.

(4) Conte, D. E.; Mouyane, M.; Stievano, L.; Fraisse, B.; Sougrati, M. T.; Olivier-Fourcade, J.; Willmann, P.; Jordy, C.; Artus, M.; Cassaignon, S.; Driezen, K.; Jumas, J.-C. *J. Solid State Electrochem.* **2012**, *16*, 3837.

DOI: 10.1021/jacs.5b10295
J. Am. Chem. Soc. 2016, 138, 231−238

(5) Wandt, J.; Marino, C.; Gasteiger, H. A.; Jakes, P.; Eichel, R.-A.; Granwehr, J. *Energy Environ. Sci.* **2015**, *8*, 1358.
(6) Sathiya, M.; Leriche, J. B.; Salager, E.; Gourier, D.; Tarascon, J. M.; Vezin, H. *Nat. Commun.* **2015**, *6*, 6276.
(7) Oudenhoven, J. F. M.; Labohm, F.; Mulder, M.; Niessen, R. A. H.; Mulder, F. M.; Notten, P. H. L. *Adv. Mater.* **2011**, *23*, 4103.
(8) Soni, K. K.; Williams, D. B.; Newbury, D. E.; Chi, P.; Downing, R. G.; Lamaza, G. *Corrosion* **1993**, *49*, 31.
(9) Liu, D. X.; Wang, J.; Pan, K.; Qiu, J.; Canova, M.; Cao, L. R.; Co, A. C. *Angew. Chem., Int. Ed.* **2014**, *53*, 9498.
(10) Downing, R. G. *Rev. Sci. Instrum.* **2014**, *85*, 045109.
(11) Wang, J.; Liu, D. X.; Canova, M.; Downing, R. G.; Cao, L. R.; Co, A. C. *J. Radioanal. Nucl. Chem.* **2014**, *301*, 277.
(12) He, Y.; Downing, R. G.; Wang, H. *J. Power Sources* **2015**, *287*, 226.
(13) Zhang, X.; Verhallen, T. W.; Labohm, F.; Wagemaker, M. *Adv. Energy Mater.* **2015**, *5*, 1500498.
(14) Downing, R. G.; Lamaze, G. P.; Langland, J. K.; Hwang, S. T. *J. Res. Natl. Inst. Stand. Technol.* **1993**, *98*, 109.
(15) Whitney, S.; Biegalski, S. R.; Huang, Y. H.; Goodenough, J. B. *J. Electrochem. Soc.* **2009**, *156*, A886.
(16) Starke, E. A.; Sanders, T. H.; Palmer, I. G. *J. Met.* **1981**, *33*, 24.
(17) Powell, J. R.; Miles, F. T.; Aronson, A.; Winsche, W. E.; Bezler, P. *Nucl. Fusion* **1974**, 343.
(18) Moore, J. T.; Turns, S. R.; Yetter, R. A. *Combust. Sci. Technol.* **2005**, *177*, 627.
(19) Dey, A. N. *J. Electrochem. Soc.* **1971**, *118*, 1547.
(20) Rao, B. M. L.; Francis, R. W.; Christopher, H. A. *J. Electrochem. Soc.* **1977**, *124*, 1490.
(21) Limthongkul, P.; Jang, Y.-I.; Dudney, N. J.; Chiang, Y.-M. *J. Power Sources* **2003**, *119*−*121*, 604.
(22) Wang, Z.; Gu, M.; Zhou, Y.; Zu, X.; Connell, J. G.; Xiao, J.; Perea, D.; Lauhon, L. J.; Bang, J.; Zhang, S.; Wang, C.; Gao, F. *Nano Lett.* **2013**, *13*, 4511.
(23) Liu, X. H.; Huang, S.; Picraux, S. T.; Li, J.; Zhu, T.; Huang, J. Y. *Nano Lett.* **2011**, *11*, 3991.
(24) Kushima, A.; Liu, X. H.; Zhu, G.; Wang, Z. L.; Huang, J. Y.; Li, J. *Nano Lett.* **2011**, *11*, 4535.
(25) Liu, H.; Strobridge, F. C.; Borkiewicz, O. J.; Wiaderek, K. M.; Chapman, K. W.; Chupas, P. J.; Grey, C. P. *Science* **2014**, *344*, 1252817-1−1252817-7.
(26) Delacourt, C.; Poizot, P.; Tarascon, J.-M.; Masquelier, C. *Nat. Mater.* **2005**, *4*, 254.
(27) Ravnsbæk, D. B.; Xiang, K.; Xing, W.; Borkiewicz, O. J.; Wiaderek, K. M.; Gionet, P.; Chapman, K. W.; Chupas, P. J.; Chiang, Y. M. *Nano Lett.* **2014**, *14*, 1484.
(28) Niu, J.; Kushima, A.; Qian, X.; Qi, L.; Xiang, K.; Chiang, Y.-M.; Li, J. *Nano Lett.* **2014**, *14*, 4005.
(29) Zhang, X.; van Hulzen, M.; Singh, D. P.; Brownrigg, A.; Wright, J. P.; van Dijk, N. H.; Wagemaker, M. *Nat. Commun.* **2015**, *6*, 8333.
(30) Li, Y.; El Gabaly, F.; Ferguson, T. R.; Smith, R. B.; Bartelt, N. C.; Sugar, J. D.; Fenton, K. R.; Cogswell, D. A.; Kilcoyne, A. L. D.; Tyliszczak, T.; Bazant, M. Z.; Chueh, W. C. *Nat. Mater.* **2014**, *13*, 1149.
(31) Zhang, X.; van Hulzen, M.; Singh, D. P.; Brownrigg, A.; Wright, J. P.; van Dijk, N. H.; Wagemaker, M. *Nano Lett.* **2014**, *14*, 2279.
(32) Bai, P.; Cogswell, D. A.; Bazant, M. Z. *Nano Lett.* **2011**, *11*, 4890.
(33) Xia, Y. Y.; Sakai, T.; Fujieda, T.; Yang, X. Q.; Sun, X.; Ma, Z. F.; McBreen, J.; Yoshio, M. *J. Electrochem. Soc.* **2001**, *148*, A723.
(34) Downing, R. G. *Trans. Am. Nucl. Soc.* **2013**, *109*, 527.
(35) Biallozor, S.; Lieder, M. *J. Electrochem. Soc.* **1993**, *140*, 2537.
(36) Maskell, W. C.; Owen, J. R. *J. Electrochem. Soc.* **1985**, *132*, 1602.
(37) Lantelme, F. *J. Electroanal. Chem. Interfacial Electrochem.* **1985**, *191*, 343.
(38) Zhu, X.; Schoenitz, M.; Dreizin, E. L. *J. Alloys Compd.* **2007**, *432*, 111.
(39) Owen, J. R.; Maskell, W. C.; Steele, B. C. H.; Nielsen, T. S.; Sørensen, O. T. *Solid State Ionics* **1984**, *13*, 329.
(40) Harks, P.; Mulder, F. M.; Notten, P. H. L. *J. Power Sources* **2015**, *288*, 92.
(41) Liu, Y.; Hudak, N. S.; Huber, D. L.; Limmer, S. J.; Sullivan, J. P.; Huang, J. Y. *Nano Lett.* **2011**, *11*, 4188.
(42) Cullity, B. D. *Elements of X-ray Diffraction*; Addison-Wesley Publishing Company: Boston, MA, 1978.
(43) Uesugi, T.; Higashi, K. *Comput. Mater. Sci.* **2013**, *67*, 1.
(44) Wang, C. R.; Neeleshwar, S.; Chen, Y. Y.; Ho, J. C. *J. Appl. Phys.* **2003**, *94*, 7938.
(45) Yamada, A.; Koizumi, H.; Nishimura, S.-i.; Sonoyama, N.; Kanno, R.; Yonemura, M.; Nakamura, T.; Kobayashi, Y. *Nat. Mater.* **2006**, *5*, 357.
(46) Yazami, R. *Nanomaterials for Lithium-Ion Batteries: Fundamentals and Applications*; CRC Press: Boca Raton, FL, 2013.
(47) Chung, S.-Y.; Kim, Y.-M.; Kim, J.-G.; Kim, Y.-J. *Nat. Phys.* **2009**, *5*, 68.
(48) Scholz, F. *Electroanalytical Methods: Guide to Experiments and Applications*; Springer : Berlin, Heidelberg, 2010.

DOI: 10.1021/jacs.5b10295
J. Am. Chem. Soc. 2016, 138, 231−238